FLUID-STRUCTURE SIMULATIONS AND BENCHMARKING OF ARTERY ANEURYSMS UNDER PULSATILE BLOOD FLOW

Eugenio Aulisa[1], Giorgio Bornia[2] and Sara Calandrini[2]

[1] Department of Mathematics and Statistics
Texas Tech University
Lubbock, TX 79409, USA
e-mail: eugenio.aulisa@ttu.edu

[2] Department of Mathematics and Statistics
Texas Tech University
Lubbock, TX 79409, USA
e-mail: giorgio.bornia@ttu.edu, sara.calandrini@ttu.edu

Keywords: Cerebral aneurysms, Incompressible Navier-Stokes equations, Fluid-structure interaction, Intracranial stent.

Abstract. *In this paper Fluid-structure interaction (FSI) simulations of artery aneurysms are carried out where both the fluid flow and the hyperelastic material are incompressible. We focus on time-dependent formulations adopting a monolithic approach, where the deformation of the fluid domain is taken into account according to an Arbitrary Lagrangian Eulerian (ALE) scheme. The exact Jacobian matrix is implemented by using automatic differentiation tools. The system is modeled using a specific equation shuffling that assures an optimal pivoting. We propose to solve the resulting linearized system at each nonlinear outer iteration with a GMRES solver preconditioned by a geometric multigrid algorithm with an Additive Schwarz Method (ASM) smoother.*

In order to test our numerical method on possible hemodynamics applications, we describe several benchmark settings. The configurations consist of realistic artery aneurysms where hybrid meshes are employed. Both two and three-dimensional benchmarks are considered. We show numerical results for the described aneurysm geometries focusing on pulsatile inflow conditions. Parallel implementation is addressed and a case of endovascular stent implantation on a cerebral aneurysm is presented.

1 INTRODUCTION

Fluid-structure interaction (FSI) of aneurysms and, in general, the field of computational vascular and cardiovascular modeling has matured immensely over the last decade. There have been several patient-specific FSI simulations of aneurysms, involving both intracranial aneurysms ([7], [24], [25], [26], [28]) and AAA, namely abdominal aortic aneurysms ([12], [31], [18], [22]). Numerous advances in the simulation technology were proposed, but the majority of them involved only computational fluid dynamics (CFD). When pure CFD is used for vascular blood flow simulations, it is assumed that the vessel wall remains rigid. The rigid wall assumption does not properly reflect the elastic nature of arterial walls and the behavior of real blood vessels, since vessel walls are deformed by the action of blood flow forces and, in turn, this deformation alters the details of blood flow. For the modeling to be realistic, coupled FSI modeling must be employed. In this work we consider a monolithic coupling between the fluid and the solid, focusing on time-dependent formulations. Blood has been considered ad an incompressible Newtonian fluid and a hyperelastic solid has been used to represent vessel wall tissue. We describe the solid motion in a Lagrangian way, while the fluid is observed in Eulerian fashion. The deformation of the fluid domain is taken into account according to an Arbitrary Lagrangian Eulerian (ALE) approach, which is one of the most popular techniques in the FSI community ([4], [13], [23], [29]).

To linearize the FSI system, Newton linearization is performed, therefore the evaluation of the Jacobian associated to the fluid-solid coupled state equations is required. An analytic expression of the exact Jacobian may be determined using shape derivative calculus [14], but in certain cases, for simplicity or time performance, it may be more convenient to consider the use of approximate Jacobians. For this purpose, a divided difference approach may be used, as in [16].

In this work, we have chosen to compute the exact Jacobian matrix with automatic differentiation tools provided by the Adept software package ([15]), implemented in an in-house finite element library *C++ Femus library*. Automatic differentiation is a very convenient tool that requires little code modification.

To solve the linearized FSI system, we propose a monolithic Newton-Krylov solver preconditioned by a geometric multigrid algorithm. Newton linearization is performed as an outer iteration. Multigrid F-cycle and V-cycle schemes are considered with a Richardson smoother preconditioned by an additive Schwarz method (ASM). Both multigrid and domain decomposition methods draw a lot of attention within the FSI community. In [27] and [21], where hemodynamics applications are also addressed, a geometric multigrid solver with a Multilevel Pressure Schur Complement (MPSC) Vanka-like smoother is considered. In [30] a Newton-Krylov algorithm with an overlapping additive Schwarz preconditioner is considered in applications to parallel three-dimensional blood flow simulations.

For validation and evaluation of the accuracy and performance of the proposed methodology, we describe several biomedical benchmark settings. We concentrate on cerebral aneurysms, presenting numerical studies for both 2D and 3D aneurysm configurations. The 2D geometry is based on the benchmark setting proposed in [27] and [21], and the 3D shape is an extension of the 2D configuration based on a real aneurysm view proposed on [27].

We also propose simulations of stenting technology applied to the 2D and 3D geometries. For the 2D configuration, flow diverter (FD) stents with five and eleven struts have been modeled. Stents are placed on the aneurysm neck and are characterized by very thin wires ($30 - 100\mu m$). It's known in the literature ([17], [33]) that the large difference in scale between the stent struts and aneurysm neck can create technical difficulties in the mesh generation and in the conver-

gence of consequent FSI or CFD calculations. To resolve such meshing difficulties, two possible options can be explored: adaptive embedding techniques and porous medium modeling. With the former approach, vessel walls are treated with body-fitted unstructured grids, and stents are embedded in the grids; moreover, adaptive meshing refinement is performed near the stents ([10], [8]). A more recent technique simulates the effect of a FD through the use of a porous medium layer ([3], [33], [19]). Advantages of the porous medium method include the reduction of the number of simulation mesh elements, with the resulting reduction of computational time. In this paper, we decided to model a FD as a porous medium and, for the 2D configuration, we compared the results with the previous mentioned cases, where stents with five and eleven struts have been considered. In the 3D geometry, the porous medium approach has been used as well to simulate the effect of a FD. To the authors knowledge, the present study is the first of its kind that performs FSI computations in a stented cerebral aneurysm where the the flow diverter is modeled as a porous medium.

The paper is organized as follows. In Section 2 we present the strong formulations of the time-dependent incompressible FSI problems under investigation. In section 3 describe our Monolithic Newton-Krylov solver, illustrating the features of the multigrid preconditioner with domain decomposition smoothing. Numerical results of benchmark problems are presented in Sections 4 and 5. Finally, we draw our conclusions.

2 FORMULATION OF THE FSI PROBLEM

Let $\Omega_t = \Omega_t^f \cup \Omega_t^s \subset \mathbb{R}^n$ be the current configuration of fluid and solid at time t and let $\widehat{\Omega} = \widehat{\Omega}^f \cup \widehat{\Omega}^s \subset \mathbb{R}^n$ be a reference configuration. Clearly, $\widehat{\Omega}^f, \Omega_t^f$ and $\widehat{\Omega}^s, \Omega_t^s$ are referred to fluid and solid, respectively. Any reference configuration can be equivalently chosen in principle. The natural choice is the initial configuration, $\Omega_0 = \widehat{\Omega}$.

Let $\Gamma_t^i = \Omega_t^f \cap \Omega_t^s$ and $\widehat{\Gamma}^i = \widehat{\Omega}^f \cap \widehat{\Omega}^s$ be the interface between solid and fluid in the current and reference configuration, respectively. Moreover, we define the parts of the boundary adjacent only to the fluid or only to the solid as Γ_t^f, Γ_t^s and $\widehat{\Gamma}_t^f$, $\widehat{\Gamma}_t^s$ in the current configuration and reference configuration, respectively. In the following we will use the notations $\widehat{\nabla}$ or ∇ to refer to the gradient operators and the symbols $\widehat{\mathbf{n}}$ or $\mathbf{n}$ to denote the outward unit normal fields in the reference or in the current configuration, respectively.

For every domain $D_t \subset \mathbb{R}^n$ (which may change in time), we also define the cylinder Q_{D_t} as

$$Q_{D_t} = \{(\mathbf{x}, t) \text{ s.t. } \mathbf{x} \in D_t, t \in [0, T]\}. \tag{1}$$

The domains $\{\widehat{\Omega}^s, Q_{\widehat{\Omega}^s}\}$ are called *Lagrangian domains* and the fields $q^s(\widehat{\mathbf{x}})$ or $q^s(\widehat{\mathbf{x}}, t)$ defined on them are called *Lagrangian fields*. The domain $\widehat{\Omega}^s$ is initially occupied by the solid we observe. We follow the motion of the solid in a Lagrangian way. The domains $\{\widehat{\Omega}^f, Q_{\widehat{\Omega}^f}\}$ are called *ALE domains* and the fields $q^f(\widehat{\mathbf{x}})$ or $q^f(\widehat{\mathbf{x}}, t)$ defined on them are called *ALE fields*. The domain $\widehat{\Omega}^f$ is the domain on which we initially observe the fluid motion in a Eulerian way.

As a consequence of the solid movement, the domain on which we observe the fluid motion changes in time as well, so that we need to define a deformation for the fluid domain. The domain Ω_t^f is occupied only by fluid at each time t. The moving domains Ω_t^f and Ω_t^s and the corresponding cylinders are called *Eulerian domains*, and fields $q(\mathbf{x})$ or $q(\mathbf{x}, t)$ defined on Eulerian domains are called *Eulerian fields*. Notice that the Eulerian cylinder has a variable base in time.

In order to describe the motion of the fluid and solid domains, let us define a t-parametrized family of invertible and sufficiently smooth mappings $\mathcal{X}_t$ of the reference configuration $\widehat{\Omega}$ to the

deformed ones Ω_t, so that

$$\mathcal{X}_t : \widehat{\Omega} \to \Omega_t \,, \quad \mathcal{X}_t(\widehat{\mathbf{x}}) := \widehat{\mathbf{x}} + \mathbf{d}(\widehat{\mathbf{x}}, t) \,. \tag{2}$$

The field $\mathbf{d}(\widehat{\mathbf{x}}, t)$ is called *displacement field*. The displacement field $\mathbf{d}(\widehat{\mathbf{x}}, t)$ is determined separately in the fluid and solid parts as a solution of two different subproblems. Its restrictions $\mathbf{d}^f(\widehat{\mathbf{x}}, t)$ and $\mathbf{d}^s(\widehat{\mathbf{x}}, t)$ are referred to as *fluid domain displacement* (or *ALE displacement*) and *solid displacement*, respectively. They are required to take on common values at the interface, namely

$$\mathbf{d}^s(\widehat{\mathbf{x}}, t) = \mathbf{d}^f(\widehat{\mathbf{x}}, t) \,, \quad \widehat{\mathbf{x}} \in \widehat{\Gamma}^i \,. \tag{3}$$

For every $(\widehat{\mathbf{x}}, t) \in Q_{\widehat{\Omega}}$, we also define

$$\mathbf{F}(\mathbf{d}(\widehat{\mathbf{x}}, t)) = \widehat{\nabla} \mathcal{X}_t(\widehat{\mathbf{x}}) = I + \widehat{\nabla} \mathbf{d}(\widehat{\mathbf{x}}, t) \,, \tag{4}$$

$$J(\mathbf{d}(\widehat{\mathbf{x}}, t)) = \det \mathbf{F}(\mathbf{d}(\widehat{\mathbf{x}}, t)) \,, \tag{5}$$

$$\mathbf{B}(\mathbf{d}(\widehat{\mathbf{x}}, t)) = \mathbf{F}(\mathbf{d}(\widehat{\mathbf{x}}, t)) \mathbf{F}^T(\mathbf{d}(\widehat{\mathbf{x}}, t)) \,. \tag{6}$$

The symbols $\mathbf{F}$ and $\mathbf{B}$ denote the *deformation gradient tensor* and the *left Cauchy-Green deformation tensor*, respectively.

2.1 The solid subproblem

Let $(\mathbf{d}^s(\widehat{\mathbf{x}}, t), p^s(\widehat{\mathbf{x}}, t))$ be the displacement and the pressure state variables in the solid domain. The *solid subproblem* consists in determining the variables $(\mathbf{d}^s, p^s)$ as solutions of

$$\rho^s \frac{\partial^2 \mathbf{d}^s}{\partial t^2} - \nabla \cdot \boldsymbol{\sigma}^s(\mathbf{d}^s, p^s) - \rho^s \mathbf{f}^s = \mathbf{0}, \quad (\mathbf{x}, t) \in Q_{\Omega_t^s} \,, \tag{7}$$

$$J(\mathbf{d}^s) - 1 = 0 \,, \quad (\widehat{\mathbf{x}}, t) \in Q_{\widehat{\Omega}^s} \,, \tag{8}$$

$$\boldsymbol{\sigma}^s(\mathbf{d}^s, p^s) \cdot \mathbf{n}^s - \boldsymbol{\sigma}^f(\mathbf{u}^f, p^f) \cdot \mathbf{n}^f = 0 \,, \quad (\mathbf{x}, t) \in Q_{\Gamma_t^i} \,, \tag{9}$$

$$\mathcal{B}_t^s(\mathbf{d}^s, p^s) = \mathbf{0} \,, \quad (\mathbf{x}, t) \in Q_{\Gamma_t^s} \,, \tag{10}$$

$$\mathbf{d}^s(\widehat{\mathbf{x}}, 0) = \mathbf{0} \,, \quad \widehat{\mathbf{x}} \in \widehat{\Omega}^s \equiv \Omega_{t=0}^s \,, \tag{11}$$

$$\frac{\partial \mathbf{d}^s}{\partial t}(\widehat{\mathbf{x}}, 0) = \mathbf{0} \,, \quad \widehat{\mathbf{x}} \in \widehat{\Omega}^s \equiv \Omega_{t=0}^s \,. \tag{12}$$

The first two equations are known as the incompressible elasticity equations. The symbols ρ^s and $\mathbf{f}^s$ denote mass density and body force density for the solid, respectively, and $\mathcal{B}_t^s$ denotes an abstract boundary operator for the solid external boundary Γ_t^s, which may correspond to Dirichlet, Neumann or other types of boundary conditions.

We remark that the input to this solid subproblem is the stress at the interface coming from the fluid part while the output is the displacement of the solid, namely $\mathbf{d}^s$. The pressure in the solid p^s is an internal variable and it does not have a clear physical meaning. It can be regarded mathematically as the Lagrange multiplier associated to the solid incompressibility constraint. For the solid stress tensor $\boldsymbol{\sigma}^s$ we consider either incompressible Neo-Hookean or incompressible Mooney-Rivlin, whose Lagrangian description is given for every $(\widehat{\mathbf{x}}, t) \in Q_{\widehat{\Omega}^s}$ by

$$\boldsymbol{\sigma}^s_{NH}(\mathbf{d}^s, p^s) = -p^s \mathbf{I} + 2\mathbf{C_1} \mathbf{B}(\mathbf{d^s}) \,, \tag{13}$$

$$\boldsymbol{\sigma}^s_{MR}(\mathbf{d}^s, p^s) = -p^s \mathbf{I} + 2\mathbf{C_1} \mathbf{B}(\mathbf{d^s}) - 2\mathbf{C_2}(\mathbf{B}(\mathbf{d^s}))^{-1} \,, \tag{14}$$

where the constants C_1 and C_2 depend on the mechanical properties of the material.

With the given choices of stress tensors, the momentum balance is of second-order in the space derivatives, and it is also of second order in the time derivative for the displacement unknown. Therefore we introduce the *solid velocity* $\mathbf{u}^s(\widehat{\mathbf{x}}, t)$ to obtain a system of equations containing only first-order time derivatives. The solid velocity is the velocity at time t of the solid particle initially at $\widehat{\mathbf{x}}$ and it is defined as

$$\mathbf{u}^s(\widehat{\mathbf{x}}, t) = \frac{\partial \mathcal{X}_t^s(\widehat{\mathbf{x}})}{\partial t} = \frac{\partial \mathbf{d}^s(\widehat{\mathbf{x}}, t)}{\partial t}\,. \tag{15}$$

We enforced it over the solid region, including its boundary $\Gamma_t^s \cup \Gamma_t^i$.

Since the solid displacement at the interface modifies the fluid domain, we can conclude that the overall fluid-solid coupling is two-way.

2.2 The fluid subproblem

Let $(\mathbf{u}^f(\mathbf{x}, t), p^f(\mathbf{x}, t))$ be the velocity and the pressure state variables in the fluid domain. The fluid subproblem consists in searching for solutions $(\mathbf{u}^f, p^f)$ of

$$\rho^f \left(\left. \frac{\partial \mathbf{u}^f}{\partial t} \right|_{\mathcal{X}^f} + \left[(\mathbf{u}^f - \frac{\partial \mathbf{d}^f}{\partial t}) \cdot \nabla \right] \mathbf{u}^f \right) - \nabla \cdot \boldsymbol{\sigma}^f(\mathbf{u}^f, p^f) - \rho^f \mathbf{f}^f = \mathbf{0} \quad (\mathbf{x}, t) \in Q_{\Omega_t^f}\,, \tag{16}$$

$$\nabla \cdot \mathbf{u}^f = 0\,, \quad (\mathbf{x}, t) \in Q_{\Omega_t^f}\,, \tag{17}$$

$$\mathbf{u}^f = \mathbf{u}^s\,, \quad (\mathbf{x}, t) \in Q_{\Gamma_t^i}\,, \tag{18}$$

$$\mathcal{B}_t^f(\mathbf{u}^f, p^f) = \mathbf{0}\,, \quad (\mathbf{x}, t) \in Q_{\Gamma_t^f}\,, \tag{19}$$

$$\mathbf{u}^f(\mathbf{x}, 0) = \mathbf{u}_0(\mathbf{x})\,, \quad \mathbf{x} \in \Omega_{t=0}^f \equiv \widehat{\Omega}^f\,. \tag{20}$$

The first two equations are referred to as the incompressible Navier-Stokes equations. The symbols ρ^f and $\mathbf{f}^f$ denote mass density and body force density for the fluid, while $\mathcal{B}_t^s$ is an abstract boundary operator for the fluid boundary, similarly as before. The initial velocity profile is denoted as $\mathbf{u}_0(x)$. The fluid stress tensor $\boldsymbol{\sigma}^f$ for incompressible Newtonian fluid flows is given as a Eulerian field for every $(\mathbf{x}, t) \in Q_{\Omega_t^f}$ by

$$\boldsymbol{\sigma}^f(\mathbf{u}^f, p^f) = -p^f \mathbf{I} + \mu(\nabla \mathbf{u}^f + (\nabla \mathbf{u}^f)^T)\,, \tag{21}$$

where μ is the fluid viscosity. Inputs to the fluid subproblem are the displacement of the fluid domain and the solid displacement on the interface. The former is used for three different purposes: to compute the position of each point, the ALE time derivative and the fluid domain velocity. The outputs of this system are both fluid velocity and fluid pressure, which are used to compute the stress at the interface for the solid subproblem.

2.3 The subproblem for the fluid domain displacement

The *subproblem for the fluid domain displacement* consists in determining the unknown $\mathbf{d}^f(\widehat{\mathbf{x}}, t)$ as a solution of

$$\widehat{\nabla} \cdot \left(k(\widehat{\mathbf{x}})(\widehat{\nabla}\mathbf{d}^f + (\widehat{\nabla}\mathbf{d}^f)^T) \right) = \mathbf{0}\,, \quad (\widehat{\mathbf{x}}, t) \in Q_{\widehat{\Omega}^f}\,, \tag{22}$$

$$\mathbf{d}^f = \mathbf{d}^s\,, \quad (\widehat{\mathbf{x}}, t) \in Q_{\widehat{\Gamma}^i}\,, \tag{23}$$

$$\mathcal{B}_t^{fd}(\mathbf{d}^f) = \mathbf{0}\,, \quad (\widehat{\mathbf{x}}, t) \in Q_{\widehat{\Gamma}^f}\,. \tag{24}$$

5

This subproblem is also referred to as the *kinematic equation* or the *pseudo-solid mapping*, as it defines the arbitrary motion of the fluid domain as another elastic solid. We denote with $\mathcal{B}_t^{fd}$ a general boundary operator which can be chosen arbitrarily depending on the problem at hand and may also be chosen to depend on time. The function $k(\widehat{\mathbf{x}})$ may be chosen to be a piecewise-constant function discontinuous across the element boundary so that smaller elements in the mesh can be made stiffer. We use smaller elements in regions where the mesh is expected to undergo large distortions, in order not to degrade the mesh quality. The expression of $k(\widehat{\mathbf{x}})$ we consider is given by

$$k(\widehat{\mathbf{x}}) = \frac{1}{\mathrm{V}_{el(\widehat{\mathbf{x}})}}, \tag{25}$$

where V_{el} is the volume of the mesh element that contains the $\mathbf{x}$ coordinate. This subproblem receives as a sole input the displacement of the fluid-solid interface from the solid part. The displacement of the fluid domain is the output. This is used to update the ALE mapping $\mathcal{X}_t^f$, with which the ALE domain velocity and the ALE time derivative are computed in the fluid subproblem.

2.4 Intracranial stents as porous media

The porous medium is modeled by the addition of a momentum source term to the standard fluid flow equations. Following [3], we assume a simple homogeneous porous medium and express the pressure gradient using the Darcy-Forchheimer equation as

$$-\nabla p = \left(\frac{\mu}{\alpha}\mathbf{u} + \frac{1}{2}C_2\rho_f\|\mathbf{u}\|\mathbf{u}\right), \tag{26}$$

where α is the permeability, C_2 is the inertial resistance factor. These coefficients are related to the thickness of the porous media wall Δe. At a macroscopic scale and in one dimension equation (26) can be averaged to measure the pressure drop between the sides of the stent walls

$$-\frac{\Delta p}{\Delta e} = \left(\frac{\mu}{\alpha}u + \frac{1}{2}C_2\rho_f u^2\right), \tag{27}$$

or

$$-\Delta p = bu + au^2, \tag{28}$$

where u is the average velocity, and coefficients a and b depend on the aneurysm geometry that is considered. Two configurations are usually possible: one in which the stent is placed parallel to the flow and one in which is placed perpendicularly to the flow (Figure 1). These two situations are completely different if we consider the blood flow behavior from a fluid mechanics point of view. In the first geometry, low exchange of blood between the parent artery and the aneurysm cavity is observed, because the aneurysm flow is created by friction from the parent artery flow. In the second geometry, the flow hits the aneurysm dome directly, since the parent artery flow points into the aneurysm, so intense fluidic exchange between the parent artery and the aneurysm is observed. We use the coefficients a and b provided in [3], which are

$$a = 1452 \ \text{ and } \ b = 4188 \ \ \text{ for stents placed parallel to flow direction}, \tag{29}$$

$$a = 367.08 \ \text{ and } \ b = 281.35 \ \ \text{ for stents placed perpendicularly to flow direction}. \tag{30}$$

From (27) and (28), the coefficients of the permeability α and the drag factor C_2 can consequently be obtained as

$$C_2 = \frac{2a}{\rho\Delta e} \quad \text{and} \quad \alpha = \frac{\mu}{b}\Delta e. \tag{31}$$

We remark that we have two sets of coefficients, one for a stent placed parallel to the flow and the other for a stent placed perpendicularly.
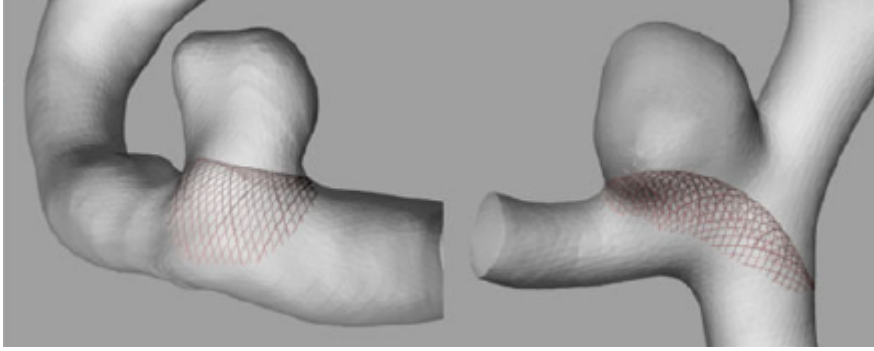

Figure 1: Flow diverter placement: stent placed parallel to the flow (right) and stent placed perpendicularly to the flow (left). Figure from [3].

3 MONOLITHIC NEWTON-KRYLOV SOLVER

In a monolithic formulation, we define three unknowns (displacement, velocity and pressure) in a piecewise fashion at each point of the Eulerian cylinder Q_{Ω_t} as

$$\mathbf{d} = \begin{cases} \mathbf{d}^s \text{ in } Q_{\Omega_t^s} \\ \mathbf{d}^i \text{ in } Q_{\Gamma_t^i} \, , \\ \mathbf{d}^f \text{ in } Q_{\Omega_t^f} \end{cases} \mathbf{u} = \begin{cases} \mathbf{u}^s \text{ in } Q_{\Omega_t^s} \\ \mathbf{u}^i \text{ in } Q_{\Gamma_t^i} \, , \\ \mathbf{u}^f \text{ in } Q_{\Omega_t^f} \end{cases} \mathbf{p} = \begin{cases} p^s \text{ in } Q_{\Omega_t^s} \\ p^f \text{ in } Q_{\Omega_t^f} \, , \end{cases}$$

enforcing continuity across the fluid-solid interface only for the displacement and the velocity. The weak formulation of the resulting system is discretized using appropriate finite element spaces and the corresponding Jacobian matrix is obtained by an exact Newton linearization implemented by automatic differentiation ([15]). The solution of the linear systems is performed using a GMRES solver preconditioned by a geometric multigrid algorithm. The smoother is of modified Richardson type, in turn preconditioned by a restricted additive Schwarz method. The coarse grid correction problem is dealt with by a direct solver of the monolithic system.

3.1 Structure of the Jacobian

For every nonlinear step k denote the exact Jacobian as $\mathbf{J}^{(k)}$. It is important to notice that the way in which the equations and the unknowns are ordered determines the block structure of $\mathbf{J}^{(k)}$, and different orderings, though equivalent mathematically, can have a significant effect on the convergence properties and computational time of the solver, especially in the parallel setting. In this work we followed a field-ordering approach as in [14], but other approaches can be used. For example, the authors in [6] ordered the equations element by element.
In the Jacobian matrix we use the symbols K for the kinematic equation (15) in the solid and on the fluid-solid interface, A for the kinematic ALE displacement equation (22) in the fluid, S for the momentum equation (7) in the solid, I for the momentum equation (9) on the fluid-solid interface, F for the momentum equation (16) in the fluid, V for the continuity equation (8) in the solid, W for the continuity equation (17) in the fluid. The Jacobian has the following block structure, and the order of the variables is listed at the top of the matrix.

Order of the unknowns: $\qquad \begin{bmatrix} \mathbf{d}^s\, \mathbf{d}^i\, \mathbf{d}^f \,\big|\, \mathbf{u}^s\, \mathbf{u}^i\, \mathbf{u}^f \,\big|\, p^s\, p^f \end{bmatrix}^{\mathsf{T}}$

$$\tag{32}$$

$$
\mathbf{J}^{(k)} =
\left[
\begin{array}{ccc|ccc|cc}
S_{\mathbf{d^s}}^{\mathbf{d^s}} & S_{\mathbf{d^i}}^{\mathbf{d^s}} & 0 & S_{\mathbf{u^s}}^{\mathbf{d^s}} & S_{\mathbf{u^i}}^{\mathbf{d^s}} & 0 & S_{p^s}^{\mathbf{d^s}} & 0 \\
I_{\mathbf{d^s}}^{\mathbf{d^i}} & I_{\mathbf{d^i}}^{\mathbf{d^i}} & I_{\mathbf{d^f}}^{\mathbf{d^i}} & I_{\mathbf{u^s}}^{\mathbf{d^i}} & I_{\mathbf{u^i}}^{\mathbf{d^i}} & I_{\mathbf{u^f}}^{\mathbf{d^i}} & I_{p^s}^{\mathbf{d^i}} & I_{p^f}^{\mathbf{d^i}} \\
0 & A_{\mathbf{d^i}}^{\mathbf{d^f}} & A_{\mathbf{d^f}}^{\mathbf{d^f}} & 0 & 0 & 0 & 0 & 0 \\
\hline
K_{\mathbf{d^s}}^{\mathbf{u^s}} & K_{\mathbf{d^i}}^{\mathbf{u^s}} & 0 & K_{\mathbf{u^s}}^{\mathbf{u^s}} & K_{\mathbf{u^i}}^{\mathbf{u^s}} & 0 & 0 & 0 \\
K_{\mathbf{d^s}}^{\mathbf{u^i}} & K_{\mathbf{d^i}}^{\mathbf{u^i}} & 0 & K_{\mathbf{u^s}}^{\mathbf{u^i}} & K_{\mathbf{u^i}}^{\mathbf{u^i}} & 0 & 0 & 0 \\
0 & F_{\mathbf{d^i}}^{\mathbf{u^f}} & F_{\mathbf{d^f}}^{\mathbf{u^f}} & 0 & F_{\mathbf{u^i}}^{\mathbf{u^f}} & F_{\mathbf{u^f}}^{\mathbf{u^f}} & 0 & F_{p^f}^{\mathbf{u^f}} \\
\hline
V_{\mathbf{d^s}}^{p^s} & V_{\mathbf{d^i}}^{p^s} & 0 & 0 & 0 & 0 & 0 & 0 \\
0 & W_{\mathbf{d^i}}^{p^f} & W_{\mathbf{d^f}}^{p^f} & 0 & W_{\mathbf{u^i}}^{p^f} & W_{\mathbf{u^f}}^{p^f} & 0 & 0 \\
\end{array}
\right]
\begin{array}{l}
\text{Momentum Solid} \\
\text{Momentum Interface} \\
\text{Kinematic fluid} \\
\text{Kinematic Solid} \\
\text{Kinematic Interface} \\
\text{Momentum Fluid} \\
\text{Continuity Solid} \\
\text{Continuity Fluid}
\end{array}
\tag{33}
$$

3.2 Geometric Multigrid preconditioner

As a preconditioner to the outer monolithic GMRES iteration, we consider the action of geometric multigrid. Consider L levels of triangulations Ω_{h_l} with associated mesh size h_l obtained recursively by simple midpoint refinement from an original geometrically conforming coarse triangulation Ω_{h_0}. The finite element spaces associated to each level triangulation Ω_{h_l} are $\boldsymbol{\Phi}(\Omega_{h_l})$ and $\Psi(\Omega_{h_l})$. The *prolongation* I_{l-1}^l and *restriction* I_l^{l-1} operators

$$I_{l-1}^l : \boldsymbol{\Phi}(\Omega_{h_{l-1}}) \times \boldsymbol{\Phi}(\Omega_{h_{l-1}}) \times \Psi(\Omega_{h_{l-1}}) \to \boldsymbol{\Phi}(\Omega_{h_l}) \times \boldsymbol{\Phi}(\Omega_{h_l}) \times \Psi(\Omega_{h_l}), \tag{34}$$

$$I_l^{l-1} : \boldsymbol{\Phi}(\Omega_{h_l}) \times \boldsymbol{\Phi}(\Omega_{h_l}) \times \Psi(\Omega_{h_l}) \to \boldsymbol{\Phi}(\Omega_{h_{l-1}}) \times \boldsymbol{\Phi}(\Omega_{h_{l-1}}) \times \Psi(\Omega_{h_{l-1}}) \tag{35}$$

are defined as

$$I_{l-1}^l \mathbf{v} = \mathbf{v}, \quad \left(I_l^{l-1}\mathbf{w}, \mathbf{v} \right) = \left(\mathbf{w}, I_{l-1}^l \mathbf{v} \right) \tag{36}$$

for all $\mathbf{v} \in \boldsymbol{\Phi}(\Omega_{h_{l-1}}) \times \boldsymbol{\Phi}(\Omega_{h_{l-1}}) \times \Psi(\Omega_{h_{l-1}})$ and $\mathbf{w} \in \boldsymbol{\Phi}(\Omega_{h_l}) \times \boldsymbol{\Phi}(\Omega_{h_l}) \times \Psi(\Omega_{h_l})$. The prolongation is the natural injection from the coarse to the fine space, while the restriction operator I_l^{l-1} is the adjoint of I_{l-1}^l with respect to the L^2 inner product. Once finite element bases are chosen, the matrix representation of the prolongation and restriction operators will be denoted with the boldface notations $\mathbf{I}_{l-1}^l$ and $\mathbf{I}_l^{l-1}$. Clearly, these matrix representations depend on the block row ordering of the Jacobian (33). In fact, the Jacobian matrices at each level $\mathbf{J}_l$ are computed as

$$\mathbf{J}_{l-1} = \mathbf{I}_l^{l-1} \mathbf{J}_l \mathbf{I}_{l-1}^l , \tag{37}$$

so that a different Jacobian structure affects the structure of $\mathbf{I}_l^{l-1}$ and $\mathbf{I}_{l-1}^l$.
The block structures of the prolongation and restriction operators are

$$
\mathbf{I}_l^{l-1} =
\left[
\begin{array}{ccc|ccc|cc}
R_{\mathbf{d^s}}^{\mathbf{d^s}} & 0 & 0 & 0 & 0 & 0 & 0 & 0 \\
R_{\mathbf{d^s}}^{\mathbf{d^i}} & R_{\mathbf{d^i}}^{\mathbf{d^i}} & 0 & 0 & 0 & R_{\mathbf{d^f}}^{\mathbf{d^i}} & 0 & 0 \\
0 & 0 & R_{\mathbf{d^f}}^{\mathbf{d^f}} & 0 & 0 & 0 & 0 & 0 \\
\hline
0 & 0 & 0 & R_{\mathbf{u^s}}^{\mathbf{u^s}} & 0 & 0 & 0 & 0 \\
0 & 0 & 0 & R_{\mathbf{u^s}}^{\mathbf{u^i}} & R_{\mathbf{u^i}}^{\mathbf{u^i}} & 0 & 0 & 0 \\
0 & 0 & 0 & 0 & 0 & R_{\mathbf{u^f}}^{\mathbf{u^f}} & 0 & 0 \\
\hline
0 & 0 & 0 & 0 & 0 & 0 & R_{p^s}^{p^s} & 0 \\
0 & 0 & 0 & 0 & 0 & 0 & 0 & R_{p^f}^{p^f} \\
\end{array}
\right] , \tag{38}
$$

$$\mathbf{I}_{l-1}^{l} = \begin{bmatrix} P_{\mathbf{d^s}}^{\mathbf{d^s}} & P_{\mathbf{d^s}}^{\mathbf{d^i}} & 0 & 0 & 0 & 0 & 0 & 0 \\ 0 & P_{\mathbf{d^i}}^{\mathbf{d^i}} & 0 & 0 & 0 & 0 & 0 & 0 \\ 0 & P_{\mathbf{d^f}}^{\mathbf{d^i}} & P_{\mathbf{d^f}}^{\mathbf{d^f}} & 0 & 0 & 0 & 0 & 0 \\ \hline 0 & 0 & 0 & P_{\mathbf{u^s}}^{\mathbf{u^s}} & P_{\mathbf{u^s}}^{\mathbf{u^i}} & 0 & 0 & 0 \\ 0 & 0 & 0 & 0 & P_{\mathbf{u^i}}^{\mathbf{u^i}} & 0 & 0 & 0 \\ 0 & 0 & 0 & 0 & P_{\mathbf{u^f}}^{\mathbf{u^i}} & P_{\mathbf{u^f}}^{\mathbf{u^f}} & 0 & 0 \\ \hline 0 & 0 & 0 & 0 & 0 & 0 & P_{p^s}^{p^s} & 0 \\ 0 & 0 & 0 & 0 & 0 & 0 & 0 & P_{p^f}^{p^f} \end{bmatrix}. \tag{39}$$

Note that in Eq. (38) the entry $(2,3)$ has been moved to $(2,6)$, and the entry $(3,2)$ has been zeroed. In each sub-block the restriction operator is constructed in the usual way by evaluating coarse shape functions at fine nodes, while the prolongator is the transpose of the restriction.

3.3 Richardson-Schwarz smoother

Here we define the smoother of the multigrid algorithm. The coupled FSI system is treated in a monolithic manner at all stages, except in the smoothing process. We first partition the whole domain into the fluid and solid subregions, and then we further divide each subregion into smaller non-overlapping blocks $\Omega_k, k = 1, ..., N$. On each subdomain Ω_k we construct a subdomain preconditioner $\mathbf{B_k}$, which is a restriction of the Jacobian matrix $\mathbf{J}$, that is, it contains entries from $\mathbf{J}$ corresponding to the degrees of freedom contained in the corresponding subdomain Ω_k. In each block the equations to be solved are taken following a Vanka-type strategy. The DOFs associated to an element consist of displacement, velocity and pressure. The exchange of information between blocks is guaranteed by the fact that the support of the test function associated to the displacement and velocity DOFs extends to the neighboring elements. In a restricted additive Schwarz algorithm ([6]) the overlap is initially used to provide information to the subdomain solver, but then the result of that computation is discarded in the overlap region. The restricted version of the additive Schwarz (ASM) preconditioner used in the Richardson scheme for the FSI Jacobian system is

$$\mathbf{B^{-1}} = \sum_{\mathbf{k=1}}^{\mathbf{N}} (\mathbf{R_k^0})^{\mathbf{T}} \mathbf{B_k^{-1}} (\mathbf{R_k^{\delta}}). \tag{40}$$

With $\mathbf{R_k}$ we indicate a restriction matrix which maps the global vector of degrees of freedom to those belonging to the subdomain Ω_k. Furthermore, $\mathbf{R_k^0}$ is a restriction matrix that does not include the overlap while $\mathbf{R_k^{\delta}}$ does.
Various inexact additive Schwarz preconditioners can be constructed by replacing the $\mathbf{B_k}$ matrices with ones that are convenient or inexpensive to compute.

4 FSI BENCHMARKING: 2D SIMULATIONS

The following 2D simulations of a cerebral aneurysm are based on a 2D hemodynamics model problem from [27]. The geometry consists of a channel (lumen of the artery) of diameter $2\,mm$ with a wall thickness of $0.25\,mm$ (Figure 2). The aneurysm wall is typically thinner than that of the healthy artery part, therefore the aneurysm has a wall thickness of $0.125\,mm$. We start by considering a mesh without stents, and then move to three cases where such devices are included. In the second and third configuration, stents are represented as in [27], that is as
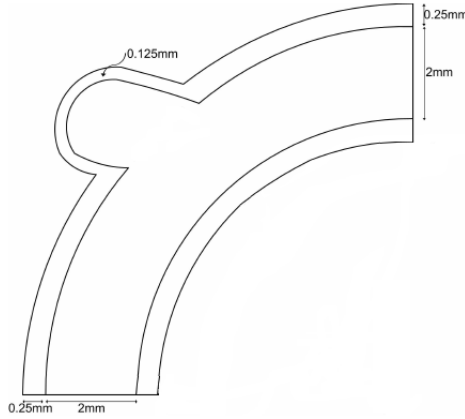
Figure 2: 2D aneurysm geometry. Figure from [27]

circular shape, placed on the neck of the aneurysm. Stents are flexible, self-expanding porous tubular meshes made of stainless steel or other alloys and are characterized by very thin wires $(30 - 100 \, \mu m)$. In 2D, flow diverters can be simplified as cutplanes from 3D configurations, so as circular shapes. We conclude our simulations with a case where a stent is modeled as a porous medium.

Figure 3 shows the four configurations we described. The difference between the second and third geometry is in the number of struts that compose the stent, to be precise five and eleven struts, respectively. In both cases, the wires (circular shapes) have a diameter of approximately $60 \, \mu m$. In the last configuration, the porous medium strip placed on the neck of the aneurysm has a width of approximately $60 \, \mu m$ as well ($\Delta e = 60 \, \mu m$). Since the stent is placed parallel to the flow, we know from section 2.4 that the coefficients used to represent the pressure drop in the porous media approach are $a = 1452$ and $b = 4188$.

In all cases, hybrid meshes are employed. Quads are mainly used to mesh the channel and the arterial wall of the geometry, while triangles are employed in the aneurysm bulge.

4.1 Mechanical properties and boundary conditions

Although the blood is known to be non-Newtonian in general, several studies, like [7], [11], [31], [26], [19], [27] and [20], assume it to be Newtonian, as we do in this paper. Cebral, et al. show in [9] that, for cerebral aneurysms, treatment of blood as Newtonian does not alter the computational results compared to treating it as non-Newtonian. The density and viscosity of the blood are set to $1035 \, kg/m^3$ and $3.5 \times 10^{-3} \, Pa \cdot s$, respectively. Parameter values for the elastic artery in the described model are as follows: the density of the arterial wall is $1120 \, kg/m^3$, the Young modulus and Poissons ratio are set to $1.0 \, MPa$ and 0.5, respectively. In the simulation concerning the porous medium, we considered its width (thickness in 3D) to be $60 \, \mu m$. With these parameters, the coefficients of the permeability α and the drag factor C_2 are

$$\alpha = 5.014 \cdot 10^{-11} \text{ and } C_2 = 4.676 \cdot 10^4 \ .$$

Hence, we expect a high resistance and a very low permeability.

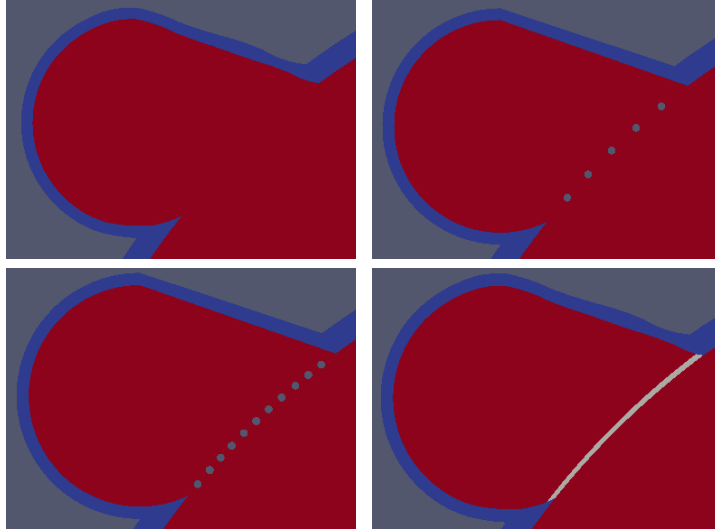The inflow boundary conditions are specified as a pulsatile velocity profile moving from the

Figure 3: 2D Configurations: no stents (top left), stent with five struts (top right), stent with eleven struts (bottom left), stent modeled as a porous medium (bottom right).

right to the left part of the channel prescribed [27]

$$v^f(t, 0, y) = v^f(0, y)(1 + 0.75 \sin(2\pi t)) \, , \tag{41}$$

where $v^f(0, y)$ is defined as parabolic inflow, namely

$$v^f(0, y) = 0.05 \, (y - 6)(y - 8). \tag{42}$$

Pressure conditions representing the resistance due to the peripheral arterial network are not taken into account in this 2D model, therefore $p = 0$ has been imposed as outflow condition at the lower left part of the artery. The no-slip condition is prescribed for the fluid on the other boundary parts. The boundary displacements at the inlet and outlet of the artery are set to zero.

4.2 Numerical results

In all the four simulations we performed, we considered the same physical parameters and boundary conditions. Figures 4 and 5 show the changes of volume and pressure in the aneurysm dome for all four cases. Pictures clearly show the given pulsatile sinusoidal behavior. In all three stent cases volume and pressure have been reduced compared with the non-stent case, which is what we expected. The five struts configuration (blue curve) is the one that allows a greater decrease in both volume and pressure. We see that doubling the number of struts (black curve) the maximum value reached by the volume increases by 50% compared to the previous case, while the maximum value for the pressure increases by 33%. This is suggesting that for a given aneurysm geometry, stents with different designs may give different results. In the past years, stents optimization techniques have already been investigated. In [2] stent design based on the combination of Lattice Boltzmann flow simulations and Simulated Annealing optimization was developed for a 2D ideal aneurysm geometry. In [33] two clinical cases have been investigated and adjustments on the stent structure and porosity are suggested to improve the fluid diverter treatment outcomes. Figure 6 shows the pressure distribution at $t = 2.156 \, s$ for the 5 and 11 struts configurations. The two distributions are very different. For the 5 struts geometry, the highest pressure point is located on the aneurysm neck, but in the aneurysm dome the pressure
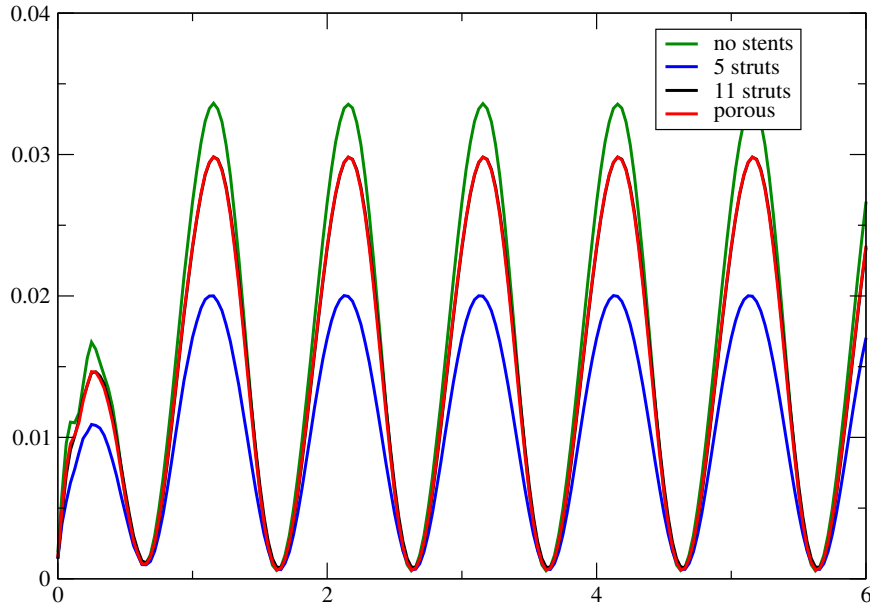
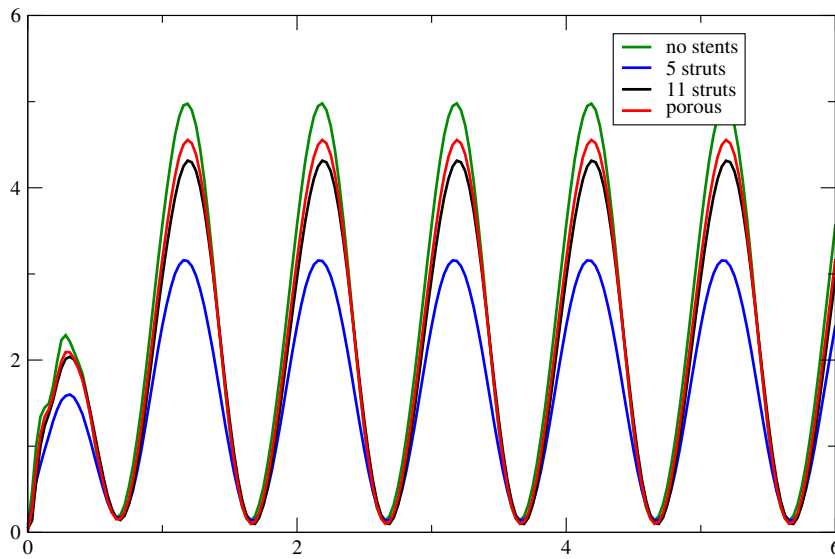Figure 4: 2D Simulations: Difference in Volume.

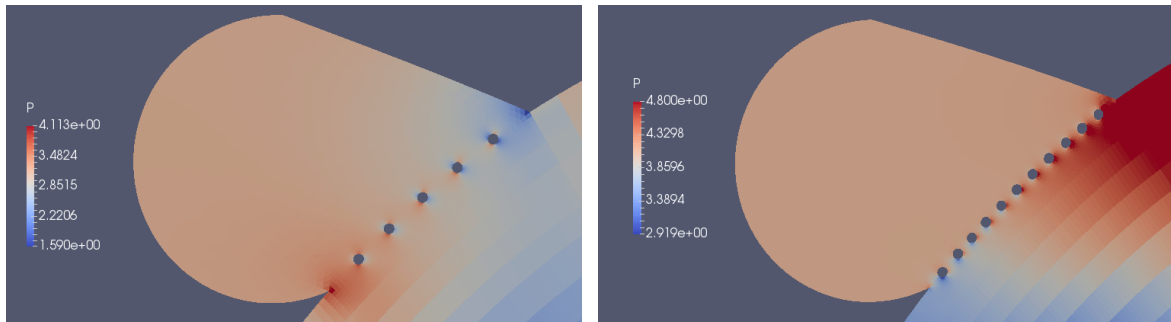Figure 5: 2D Simulations: Average Pressure.

Figure 6: 2D Configurations: pressure distribution at $t = 2.156\,s$ for the five struts stent configuration (right), pressure distribution at $t = 2.156\,s$ for the eleven struts stents configuration (left).
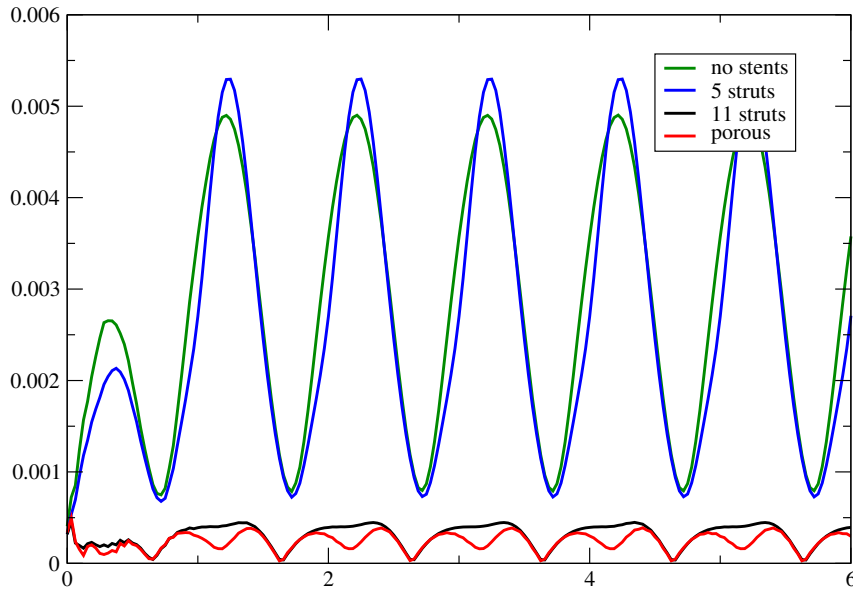
Figure 7: 2D Simulations: Average Velocity.

is much lower. For the 11 struts configuration, we have that the pressure distribution is much more uniform. The entire aneurysm dome is uniformly subjected to the same pressure value.

We also observe an analogy between the eleven struts configuration and the porous medium case (red and black curves). In Figure 4 the curves even overlap for the most part. This analogy is also found in the average velocities, which are displaced in Figure 7 . For both configurations, the average velocities are quite similar and much lower than the velocities obtained in the no stents and five struts cases. The similarity between the porous medium case and the 11 struts configuration shows the validity of the porous medium approach. Similarly to what we observed in the previous graphs, the five struts configuration keeps behave differently from the 11 strut and the porous medium configurations. The velocity distribution in the aneurysm dome after placing a stent with five wires is comparable to the one obtained without any stent. Looking
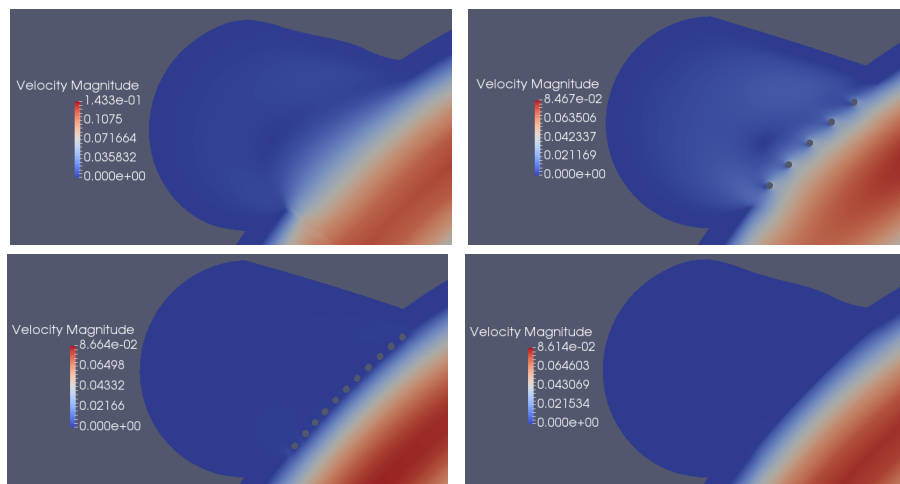
Figure 8: Magnitude Velocity at $t = 5.25\,s$ for the four 2D Configurations: no stents (top left), stent with five struts (top right), stent with eleven struts (bottom left), stent modeled as a porous medium (bottom right).

13

carefully at the flow behavior, Figure 8 shows the velocity magnitude at the aneurysm neck and dome for all four configurations. Due to the different flow rate into the aneurysm, significant local differences can be observed. As we pointed out, the porous medium case resembles the real stent configuration with 11 wires.

5 FSI BENCHMARKING: 3D SIMULATIONS

The cerebral aneurysm considered in this section (Figure 9) is a 3D extension of the 2D geometry analyzed above. To make the shape more realistic, changes have been made to the aneurysm dome, based on a real aneurysm view proposed in [27]. We assumed the aneurism wall to be uniform and equal to $0.25\,mm$. We start by considering a mesh without stents, and then move to a case where such devices are included. In this work, we decided to model the flow diverter as a porous medium. For 3D geometries, flow diverters are very difficult to simulate because the large difference of scale between the size of the flow diverters struts and the aneurysm (up to $30\,mm$) creates difficulties in the mesh process and, consequently, the simulation accuracy may be compromised. To resolve this issue, Augsburger et al. (2011) introduced the concept of employing porous media to simulate a stent ([3]). By placing a porous medium in the aneurysm neck, a unified mesh can be generated, which reduces the associated computational load. In our configuration, the porous medium disk placed on the neck of the aneurysm (Figure 9) has a thickness of approximately $112\,\mu m$ ($\Delta e = 112\,\mu m$).

In both our geometries (with and without stents), hybrid meshes are employed. Wedges are needed to mesh the artery lumen, and hexes are used for the arterial wall. Tets are mainly employed in the aneurysm dome.

5.1 Mechanical properties and boundary conditions

In these 3D simulations, for the blood flow we are using the same physical parameters used in the 2D cases. For the elastic artery wall, we decided to consider a smaller value for the Young modulus. Young modulus parameters usually vary from 0.4 to $10\,MPa$, but to clearly see the artery and the aneurysm pulse we considered $0.012\,MPa$ as our Young modulus value.

In the simulation concerning the porous medium, we considered its thickness to be $112\,\mu m$. With this value, the coefficients of the permeability α and the drag factor C_2 are
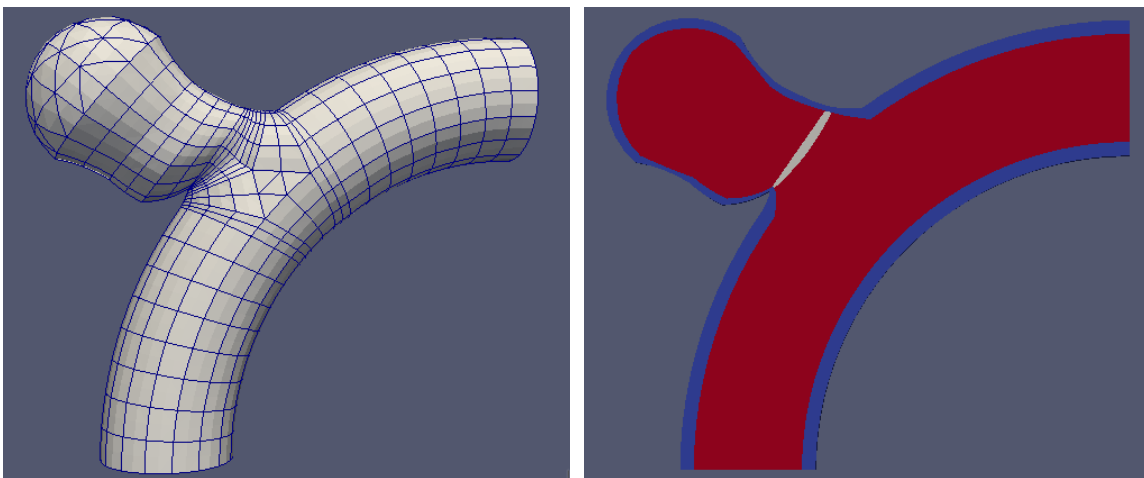

Figure 9: 3D Configurations: geometry with mesh (left), section of the 3D geometry to show the porous medium disk that simulates the intracranial stent.

$$\alpha = 9.360 \cdot 10^{-11} \text{ and } C_2 = 2.505 \cdot 10^4 \ .$$

At the inlet we specified a pulsatile flow with a period of $0.71 \ s$. The flow rate was set to a pulsatile velocity profile described by the Womersley formulation ([32]):
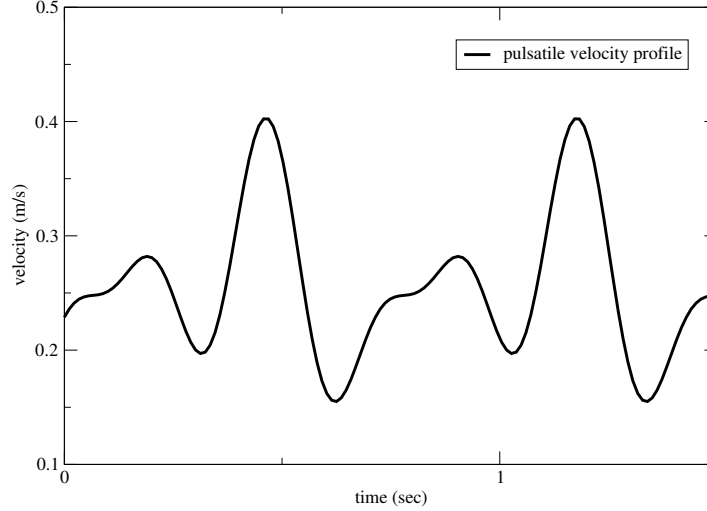
Figure 10: 3D Simulations: Velocity Profile.

$$v(r,t) = \frac{2B_0}{\pi R^2}\left[1 - \left(\frac{r}{R}\right)^2\right] + \sum_{n=1}^{N}\frac{B_n}{\pi R^2}\left[\frac{1 - \dfrac{J_0(\alpha_n\frac{r}{R}i^{3/2})}{J_0(\alpha_n i^{3/2})}}{1 - \dfrac{2J_1(\alpha_n i^{3/2})}{\alpha_n i^{3/2}J_0(\alpha_n i^{3/2})}}\right]e^{in\omega t} \ . \tag{43}$$

Here r represents the cylindrical coordinate, R denotes the radius of the inlet cross section and t is time. J_0 and J_1 are Bessel functions of the first kind of order 0 and 1. We consider

$$\alpha_n = R\sqrt{\frac{n\omega}{\nu}} \quad , \quad \alpha = R\sqrt{\frac{\omega}{\nu}} \tag{44}$$

where ω is based on one cardiac cycle ($= 0.71 \, s$) and ν indicates the kinematic viscosity. The non-dimensional parameter α is known as the *Womersley number*. The coefficients B_n are derived in reference to the chosen velocity waveform. Figure 10 shows the velocity profile v considered in our simulations. At the outlet, pressure conditions representing the resistance due to the peripheral arterial network are not taken into account, therefore $p = 0$ has been imposed as outflow condition at the lower left part of the artery. The boundary displacements at the inlet and outlet of the artery are set to zero.

5.2 Numerical results

In both simulations we performed, we considered the same physical parameters and boundary conditions. Figures 11 and 12 show the changes of volume and pressure in the aneurysm dome for the considered cases. Pictures show the waveform we gave in the Womersley formulation. We observe that, for $E = 0.012 \, MPa$, both volume and pressure have been reduced once the porous medium stent has been applied, as for the 2D case.

15
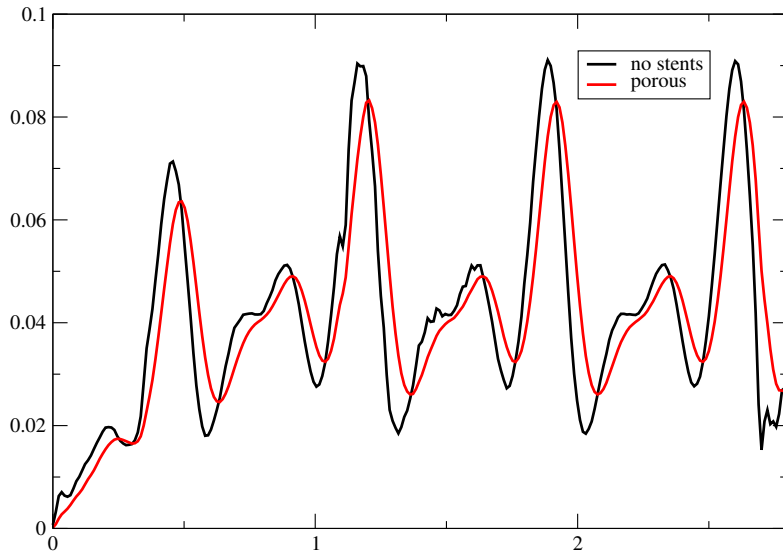
Figure 11: 3D Simulations: Relative Difference in Volume.
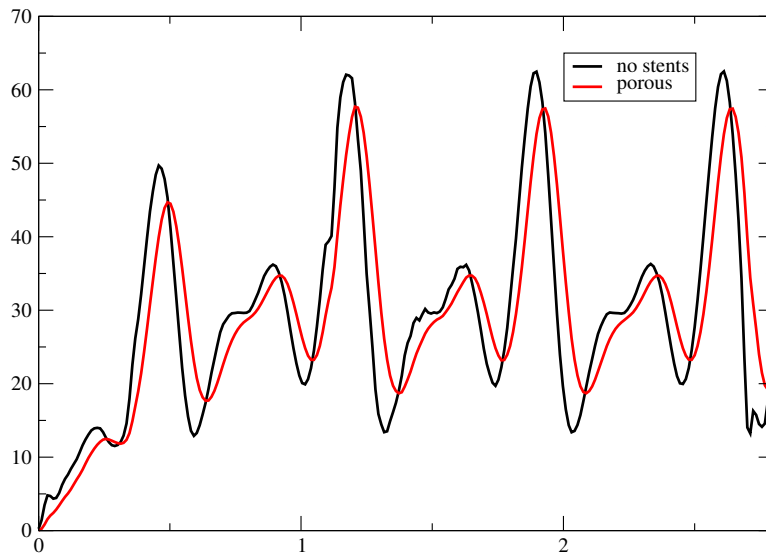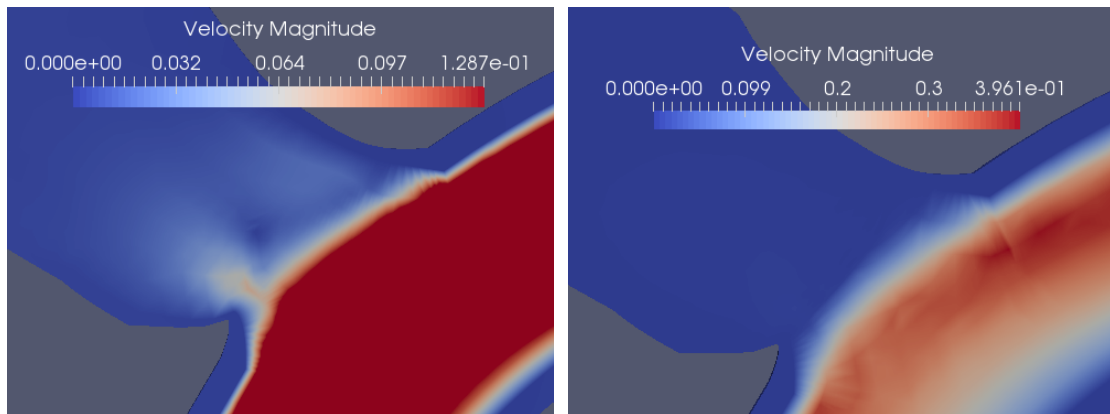

Figure 12: 3D Simulations: Average Pressure.

Figure 13: Magnitude Velocity at $t = 1.161\,s$ for the 3D Configurations: no stents (left), porous medium approach (right)

16

The velocity magnitudes at the aneurysm neck and dome at the acceleration phase ($t = 1.161\,s$) are shown in Figure 13. As we observed for the 2D setting, the flow rate changes after the porous medium placement causing a reduction of the velocity magnitude on the aneurysm neck and dome. Therefore the porous medium approach performs well also in a FSI environment.

6 CONCLUSIONS

In this paper we focused on the numerical simulation of FSI problems regarding artery aneurysms. We presented a monolithic ALE formulation assuming the fluid flow and the hyperelastic material to incompressible. We described the Newton-Krylov solver we employed where we considered the use of geometric multigrid preconditioners. We described the structure of the geometric multigrid operators, for which modified Richardson smoothers were chosen, preconditioned by an additive Schwarz algorithm of overlapping restricted type. We applied the presented numerical techniques to FSI benchmarking settings which allowed the validation of our approach for hemodynamics problems. The configurations, both two and three-dimensional, consisted of artery aneurysms where hybrid meshes are employed. The numerical results confirmed the stability and numerical efficiency of the FSI algorithm.

Our solver has been implemented in the open-source *C++ Femus library* using the GMRES solver and the geometric multigrid preconditioner interface implemented in the PETSc toolkit [5]. Looking at parallelization, PETSc offers a parallel implementation of the GMRES linear solver, so that the parallelization work for the user is left to the multigrid preconditioner part. For the direct solver, we employed the implementation of the MUMPS package [1] which includes a serial and a parallel version. For the smoother, we adopt an ASM- preconditioned Richardson method for which the parallelization is based on the domain decomposition.

From our simulations, we observe that the modelization of a flow diverter as a porous medium is successful in a FSI environment. Both in the 2D and 3D case, the aneurysm volume, pressure and velocity decrease once the porous medium stent has been placed. In the 2D simulations, the similarity between this type of modeling and the 11 struts configuration shows the validity of the porous medium approach. The different results obtained with the 5 and 11 struts configurations highlight the prominent design dependence on flow diverters performances. We also tested the porous medium approach in a 3D configuration and verified its efficiency in a FSI environment.

In our future work, we will further investigate how to choose the porosity coefficients for any general stent. A study about how to improve the pressure drop determination has already been done ([19]). Moreover, we are going to apply the porous medium approach to simulate the effect of a stent-graft in an abdominal aortic aneurysm.

REFERENCES

[1] Patrick R Amestoy, Abdou Guermouche, Jean-Yves LExcellent, and Stéphane Pralet. Hybrid scheduling for the parallel solution of linear systems. *Parallel computing*, 32(2):136–156, 2006.

[2] Hitomi Anzai, Makoto Ohta, Jean-Luc Falcone, and Bastien Chopard. Optimization of flow diverters for cerebral aneurysms. *Journal of Computational Science*, 3(1):1–7, 2012.

[3] L Augsburger, P Reymond, DA Rufenacht, and N Stergiopulos. Intracranial stents being modeled as a porous medium: flow simulation in stented cerebral aneurysms. *Annals of biomedical engineering*, 39(2):850–863, 2011.

[4] Eugenio Aulisa, Simone Bnà, and Giorgio Bornia. A monolithic ale newton-krylov solver with multigrid-richardson-schwarz preconditioning for incompressible fluid structure interaction. *Submitted to Siam Journal on Scientific Computing*, 2017.

[5] Satish Balay, J Brown, Kris Buschelman, Victor Eijkhout, W Gropp, D Kaushik, M Knepley, L Curfman McInnes, B Smith, and Hong Zhang. Petsc users manual revision 3.3. *Computer Science Division, Argonne National Laboratory, Argonne, IL*, 2012.

[6] Andrew T Barker and Xiao-Chuan Cai. Scalable parallel methods for monolithic coupling in fluid–structure interaction with application to blood flow modeling. *Journal of computational physics*, 229(3):642–659, 2010.

[7] Y Bazilevs, M-C Hsu, Y Zhang, W Wang, T Kvamsdal, S Hentschel, and JG Isaksen. Computational vascular fluid–structure interaction: methodology and application to cerebral aneurysms. *Biomechanics and modeling in mechanobiology*, 9(4):481–498, 2010.

[8] JR Cebral, F Mut, M Raschi, E Scrivano, R Ceratto, P Lylyk, and CM Putman. Aneurysm rupture following treatment with flow-diverting stents: computational hemodynamics analysis of treatment. *American journal of neuroradiology*, 32(1):27–33, 2011.

[9] Juan R Cebral, Marcelo Adrián Castro, Sunil Appanaboyina, Christopher M Putman, Daniel Millan, and Alejandro F Frangi. Efficient pipeline for image-based patient-specific analysis of cerebral aneurysm hemodynamics: technique and sensitivity. *IEEE transactions on medical imaging*, 24(4):457–467, 2005.

[10] Juan R Cebral and R Lohner. Efficient simulation of blood flow past complex endovascular devices using an adaptive embedding technique. *IEEE transactions on medical imaging*, 24(4):468–476, 2005.

[11] Paolo Crosetto, Philippe Reymond, Simone Deparis, Dimitrios Kontaxakis, Nikolaos Stergiopulos, and Alfio Quarteroni. Fluid–structure interaction simulation of aortic blood flow. *Computers & Fluids*, 43(1):46–57, 2011.

[12] ES Di Martino, G Guadagni, A Fumero, G Ballerini, R Spirito, P Biglioli, and A Redaelli. Fluid–structure interaction within realistic three-dimensional models of the aneurysmatic aorta as a guidance to assess the risk of rupture of the aneurysm. *Medical engineering & physics*, 23(9):647–655, 2001.

[13] Jean Donea, S Giuliani, and Jean-Pierre Halleux. An arbitrary lagrangian-eulerian finite element method for transient dynamic fluid-structure interactions. *Computer methods in applied mechanics and engineering*, 33(1-3):689–723, 1982.

[14] Miguel Ángel Fernández and Marwan Moubachir. A newton method using exact jacobians for solving fluid–structure coupling. *Computers & Structures*, 83(2):127–142, 2005.

[15] Robin J Hogan. Adept fast automatic differentiation library for c++: User guide.

[16] Jaroslav Hron and Stefan Turek. A monolithic fem/multigrid solver for an ale formulation of fluid-structure interaction with applications in biomechanics. In *Fluid-structure interaction*, pages 146–170. Springer, 2006.

[17] Woowon Jeong and Kyehan Rhee. Hemodynamics of cerebral aneurysms: computational analyses of aneurysm progress and treatment. *Computational and mathematical methods in medicine*, 2012, 2012.

[18] James H Leung, Andrew R Wright, Nick Cheshire, Jeremy Crane, Simon A Thom, Alun D Hughes, and Yun Xu. Fluid structure interaction of patient specific abdominal aortic aneurysms: a comparison with solid stress models. *Biomedical engineering online*, 5(1):33, 2006.

[19] Makoto Ohta, Hitomi Anzai, Yukihisa Miura, and Toshio Nakayama. Parametric study of porous media as substitutes for flow-diverter stent. *Biomaterials and Biomechanics in Bioengineering*, 2(2):111–125, 2015.

[20] Ai-Ke Qiao, Wen-Yu Fu, and You-Jun Liu. Study on hemodynamics in patient-specific thoracic aortic aneurysm. *Theoretical and Applied Mechanics Letters*, 1(1), 2011.

[21] Mudassar Razzaq, Hogenrich Damanik, Jaroslav Hron, Abderrahim Ouazzi, and Stefan Turek. Fem multigrid techniques for fluid–structure interaction with application to hemodynamics. *Applied Numerical Mathematics*, 62(9):1156–1170, 2012.

[22] Peter Rissland, Yared Alemu, Shmuel Einav, John Ricotta, and Danny Bluestein. Abdominal aortic aneurysm risk of rupture: patient-specific fsi simulations using anisotropic model. *Journal of biomechanical engineering*, 131(3):031001, 2009.

[23] Phillip A Sackinger, Peter Randall Schunk, and Rekha R Rao. A newton–raphson pseudo-solid domain mapping technique for free and moving boundary problems: a finite element implementation. *Journal of Computational Physics*, 125(1):83–103, 1996.

[24] Ryo Torii, Marie Oshima, Toshio Kobayashi, Kiyoshi Takagi, and Tayfun E Tezduyar. Fluid–structure interaction modeling of aneurysmal conditions with high and normal blood pressures. *Computational Mechanics*, 38(4):482–490, 2006.

[25] Ryo Torii, Marie Oshima, Toshio Kobayashi, Kiyoshi Takagi, and Tayfun E Tezduyar. Fluid–structure interaction modeling of a patient-specific cerebral aneurysm: influence of structural modeling. *Computational Mechanics*, 43(1):151–159, 2008.

[26] Ryo Torii, Marie Oshima, Toshio Kobayashi, Kiyoshi Takagi, and Tayfun E Tezduyar. Fluid–structure interaction modeling of blood flow and cerebral aneurysm: significance of artery and aneurysm shapes. *Computer Methods in Applied Mechanics and Engineering*, 198(45):3613–3621, 2009.

[27] Stefan Turek, J Hron, Martin Madlik, Mudassar Razzaq, Hilmar Wobker, and Jens F Acker. Numerical simulation and benchmarking of a monolithic multigrid solver for fluid-structure interaction problems with application to hemodynamics. In *Fluid Structure Interaction II*, pages 193–220. Springer, 2011.

[28] S Voß, S Glaßer, T Hoffmann, O Beuing, S Weigand, K Jachau, B Preim, D Thévenin, G Janiga, and P Berg. Fluid-structure simulations of a ruptured intracranial aneurysm: Constant versus patient-specific wall thickness. *Computational and Mathematical Methods in Medicine*, 2016, 2016.

[29] Thomas Wick. Fluid-structure interactions using different mesh motion techniques. *Computers & Structures*, 89(13):1456–1467, 2011.

[30] Hilmar Wobker and Stefan Turek. Numerical studies of vanka-type smoothers in computational solid mechanics. *Advances in Applied Mathematics and Mechanics*, 1(1):29–55, 2009.

[31] BJBM Wolters, MCM Rutten, GWH Schurink, Ursula Kose, J De Hart, and FN Van De Vosse. A patient-specific computational model of fluid–structure interaction in abdominal aortic aneurysms. *Medical engineering & physics*, 27(10):871–883, 2005.

[32] John R Womersley. Method for the calculation of velocity, rate of flow and viscous drag in arteries when the pressure gradient is known. *The Journal of physiology*, 127(3):553, 1955.

[33] Y Zhang, W Chong, and Y Qian. Investigation of intracranial aneurysm hemodynamics following flow diverter stent treatment. *Medical engineering & physics*, 35(5):608–615, 2013.